



HAL
open science

Use of composite voxels in FFT based elastic simulations of hollow glass microspheres/polypropylene composites

Romain Charière, Aldo Marano, Lionel Gélébart

► To cite this version:

Romain Charière, Aldo Marano, Lionel Gélébart. Use of composite voxels in FFT based elastic simulations of hollow glass microspheres/polypropylene composites. *International Journal of Solids and Structures*, 2020, 182-183, pp.1-14. 10.1016/j.ijsolstr.2019.08.002 . hal-02484431

HAL Id: hal-02484431

<https://hal.science/hal-02484431>

Submitted on 20 Dec 2021

HAL is a multi-disciplinary open access archive for the deposit and dissemination of scientific research documents, whether they are published or not. The documents may come from teaching and research institutions in France or abroad, or from public or private research centers.

L'archive ouverte pluridisciplinaire **HAL**, est destinée au dépôt et à la diffusion de documents scientifiques de niveau recherche, publiés ou non, émanant des établissements d'enseignement et de recherche français ou étrangers, des laboratoires publics ou privés.



Distributed under a Creative Commons Attribution - NonCommercial 4.0 International License

Use of composite voxels in FFT based elastic simulations of hollow glass microspheres/polypropylene composites

Romain Charière^a, Aldo Marano^b, Lionel Gélébart^{b,*}

^a*Univ. Grenoble Alpes, CEA, LITEN, Grenoble, 38000, France*

^b*DEN-Service de Recherches Métallurgiques Appliquées, CEA, Université Paris-Saclay, Gif-sur-Yvette F-91191, France*

Acknowledgements

We are grateful to 3M Advanced Materials Division for giving us a microspheres sample. We also wish to thank Bruno Laguitton (CEA Grenoble), Olivier Poncelet (CEA Grenoble) and Gérard Liraut (Groupe Renault) for their experimental contributions to this work and Jérémy Duvergé (internship at cea) and
5 Julien Dérouillat (cea-maison de la simulation) for their involvement in the development of the simulation software.

Complete address for the corresponding author

Lionel Gélébart

CEA Saclay

10 DEN-Service de Recherches Métallurgiques Appliquées

91191 Gif-sur-Yvette, France

Email : lionel.gelebart@cea.fr

Declaration of Interest

None

*Corresponding author

Email addresses: romain.chariere@cea.fr (Romain Charière), aldo.marano@cea.fr (Aldo Marano), lionel.gelebart@cea.fr (Lionel Gélébart)

Preprint submitted to International Journal of Solids and Structures

June 14, 2019

Use of composite voxels in FFT based elastic simulations of hollow glass microspheres/polypropylene composites

Abstract

Thermoplastic polymer composites filled with hollow glass microspheres (HGM) are of growing interest as lightweight materials. In order to better understand the relationship between the microstructure and the mechanical properties, Finite Element simulations based on the microstructure are now commonly performed. However, their computational cost becomes prohibitive when increasing the size and mesh refinement of the simulated unit cell. Massively parallel FFT-based solvers allow to overcome those limitations. The main purpose of the paper is to demonstrate that FFT-based solvers can be used to simulate HGM-thermoplastic composites, focusing on both the average behavior and the distribution of normal stresses at HGM-matrix interface. Actually, in addition to infinite elastic contrasts, the thin thickness of the HGM glass shell raises a problem, as well as the evaluation of interfacial stresses from a grid-based discretization. These problems are alleviated by using composite voxels (i.e. an homogenization rule is used for voxels crossed by an interface). The numerical study is supported by experiments (microstructure and mechanical characterization) performed on polypropylene composites with various HGM contents. Finally, an original statistical description of the interfacial normal stresses is proposed, gathering the results obtained on a large number of spheres.

Keywords: FFT simulation, Computational modelling, Mechanical properties, Polymer syntactic foam

1. Introduction

Initially, hollow fillers for polymers were used only for thermosetting matrices, but thanks to the emergence of new types of microspheres and especially the development of hollow glass microspheres (HGM) able to resist in the conditions of plastics processing industry, the manufacturing of thermoplastic matrix filled with hollow microspheres is now possible. The resulting composites are also called syntactic foams. The HGM consists of a glass shell containing an inert gas. These fillers allow to design lightweight polymers and to provide new properties of heat and phonic insulation. In the case of thermoplastic matrices, it improves the dimensional stability of part during their production and stiffens the polymers. However, for high volume fractions of microspheres, certain mechanical properties such as fracture elongation and yield strength are strongly deteriorated. This greatly limits the use of this type of material [Porfiri and Gupta (2009); Gupta

et al. (2014); Liang (2014); Çelebi (2017)].

Besides the improvement of the process, the development of a multi-scale modelling is important to understand the relationship between the microstructure and the behavior of the composite. For that purpose, the modelling should provide an estimate of the effective behavior together with a description of the local stresses and strains. On the one hand, analytical homogenization models [Nielsen (1984); Huang and Gibson (1993); Tagliavia et al. (2011); Marur (2005, 2009)] based on a reduced description of the microstructure, are efficient but they are limited to quite simple microstructures, their extension to non-linear behavior is not straightforward and they only provide a reduced description of the local quantities (per phase average in most of the cases). On the other hand, numerical simulations based on a direct description of the microstructure are much more expensive but provide the full fields of local quantities computed with non-linear material behavior. Many studies use the Finite Element Method (FEM) to simulate the thermal behavior [Liang and Li (2007)], elastic behavior and tensile strength of periodic [Sanders and Gibson (2003)] and random microstructures [Marur (2010)], effects of particles clustering and volume content on tensile properties [Yu et al. (2013); Zhang et al. (2016)] of syntactic foams. Other studies focus on the damage of syntactic foams [Bardella et al. (2014); Shams et al. (2017)], in particular by considering microspheres breaking [Panteghini and Bardella (2015)] or interfacial debonding between polymer matrix and microspheres [Cho et al. (2017)].

In the present paper, because debonding is suspected to occur at the interface between microspheres and matrix, a specific attention is paid to the distribution of interfacial normal stresses. Several authors have already investigated these stresses in various composite materials. For unidirectional composites, studies [Hojo et al. (2009); McCarthy and Vaughan (2015); Okabe et al. (2011)] have shown that distance between fibers and their alignment with loading direction significantly influence the level of interfacial stresses. Lin Weng [Weng et al. (2019)] was interested in particule size and morphology (spherical or cubic particles) influence on the interface damage and load transfers between the fillers and the matrix using a three-dimensional multi-particle finite element model. Further numerical studies on interfacial stresses in metallic syntactic foams have highlighted micromechanical phenomena, responsible for the interfacial strength and failure mechanisms of the composite [Meng and Wang (2015)], and allowed to study the stress and strain field distribution around the reinforced particules [Qi et al. (2017)].

Using standard FEM solvers, the main drawback is the computation time that explodes with the number of nodes, limiting the simulations in terms of volume size and/or mesh refinement. Conversely, FFT-based solvers [Moulinec and Suquet (1998)], developed for simulating the behavior of heterogeneous materials, have proved to be more efficient than FEM in various cases [Prakash and Lebensohn (2009); Robert and Mareau (2015)]. In addition, they are efficiently parallelized [Chen et al. (2018, 2019)] so that large-scale simulations can be performed, allowing to push back the limits observed with FEM solvers. However, their application to HGM-thermoplastic composites for estimating both the average behavior and the interfacial normal stress

45 distributions is not straightforward. First, the composite reveals very high contrasts (infinite between the gas
and the glass shell and 63 between the glass shell and the polypropylene matrix) which could induce spurious
oscillations [Gélébart and Ouaki (2015)] on the fields and convergence issues of the iterative algorithm
[Moulinec and Suquet (1998)]. Second, because the method uses a 3D grid with a uniform mesh refinement,
the fine thickness of the HGM could require a prohibitive spatial resolution to reach converged results.
50 Third, using grid-based methods for the evaluation of interfacial normal stresses appears questionable at a
first glance. Hence, the main purpose of the paper is to alleviate these issues in order to take advantage of
the great potential of FFT-based solvers for simulating HGM-thermoplastic composites.

The main ingredient allowing to tackle these questions is the use of composite voxels, proposed in linear
elasticity [Kabel et al. (2015); Gélébart and Ouaki (2015)] and extended to non-linear behaviors [Mareau
55 and Robert (2017); Kabel et al. (2017)]. It consists in using a homogenization rule for the voxels crossed by
at least one interface. The method and its application to HGM composites is introduced in section 3. An
optimization is proposed in section 4 in order to efficiently simulate the elastic response of the composite.
It is demonstrated that if composite voxels are interesting to reduce the problem size when considering the
average behavior, they are essential when considering the evaluation of interfacial normal stresses. Note
60 that the study is restricted to linear elasticity with elastic properties of glass and thermoplastic polymers.
To support the study, the microstructure and mechanical behavior of polypropylene composites, filled with
various volume fractions of iM30K (3M[®]) microspheres, are first characterized in section 2. Simulations
of random microstructures are then performed and successfully compared with experiment in section 5.
Finally, an original statistical description of the interfacial normal stresses is proposed, gathering the results
65 obtained on a large number of spheres.

2. Material

The microstructure of the studied composite is presented together with the mechanical properties of its
various components. This description will be used as an input of the numerical simulations. An experimental
investigation of tensile properties of composites is carried out for the comparison with the simulated Young's
70 moduli.

2.1. Microstructure

HGM iM30K supplied by 3M are used as the fillers in this work. The shell of microspheres is made
of soda-lime borosilicate glass. HGM density, measured by helium pycnometer, is 0.6 g.cm^{-3} . The particle
size distribution of the fillers, measured by means of a laser particule size analyzer (Mastersizer - Malvern
instruments), is shown on Fig. 1. To measure the relation between the thicknesses and diameters, a sample

of microspheres iM30K was sieved at first. HGM are separated in three batches of diameter [5-15], [15-20] and [20-50] μm . The spheres of every batch were then broken with a pestle and the thicknesses of glass fragments were measured by SEM. The increasing linear relation [Eq. 1](#) between the thickness t (μm) and the diameter d (μm) was highlighted :

$$t(d) = 0.005 \times d + 0.54 \quad (1)$$

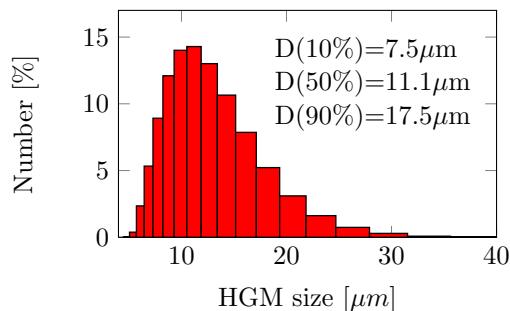


Figure 1: Size distribution graph of HGM

The thermoplastic matrix is an injection grade of polypropylene (PP) Daplen EG066AI supplied by Borealis. Dog bone tensile test specimens (width=10 mm, thickness=4 mm, length of reduced section=90 mm) are manufactured by two stages : a compounding, on a two-screw extruder (ThermoScientific) to distribute microspheres homogeneously within the polypropylene matrix and form pellets which can then be shaped by injection molding into an injection press (Billion). An example of a manufactured microstructure is observed by XRay Computed Tomography [Fig. 2](#) : the homogeneous spatial distribution of the microspheres is confirmed.

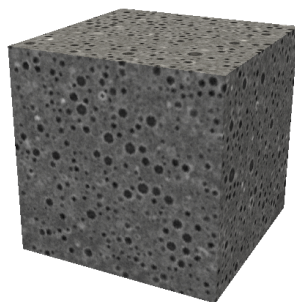


Figure 2: Tomography image of composite with 30%vol HGM

2.2. Local properties

The elastic constants used in the simulations for each phase of the composite are detailed in the [Tab. 1](#). The PP properties are determined by the measurements presented in the next section ([2.3](#)). The glass

properties used are those of a classical glass [Pedone et al. (2008)].

	Matrix (PP)	Shell (Glass)	Gas
E (MPa)	1100	69000	0
ν	0.40	0.28	0.00

Table 1: Material properties used for numerical analysis

2.3. Tensile tests on composites

The effect of HGM content on the tensile properties of the composites is determined using an Instron 55R4507 testing machine equipped with a 10 kN load cell. The strain was measured by a Provisys video system with a reference length of 90 mm. Strain rate is set to 2.10^{-4} s^{-1} . The tensile curves for various contents of HGM are drawn on Fig. 3 and the corresponding elastic moduli and ultimate stresses are gathered in Tab. 2.

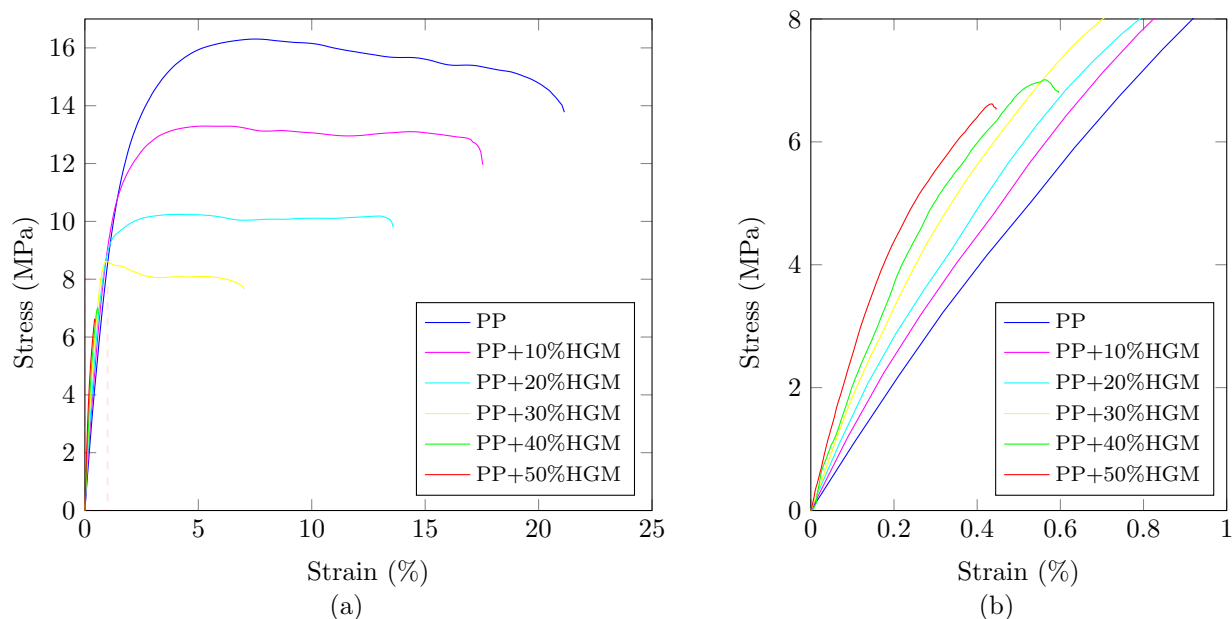


Figure 3: Macroscopic stress strain curves under tensile loading of the composites with various ratio of HGM (0, 10, 20, 30, 40, 50 %vol) (a) global curve and (b) focus on the elastic part

As expected, the density of PP/HGM composites, decreases with the increasing content of HGM. Addition of microspheres also allows to increase the Young's modulus of the composite by increasing from 1100 MPa for neat PP to 1900 MPa when it is loaded with 50%vol of HGM. However, increasing the content

	PP	PP+10%HGM	PP+20%HGM	PP+30%HGM	PP+40%HGM	PP+50%HGM
ρ (g.cm ⁻³)	0.90	0.87	0.84	0.81	0.76	0.73
E (MPa)	1100	1230	1430	1610	1730	1900
σ_{ultim} (MPa)	16.0	13.2	10.2	8.7	7.2	6.7

Table 2: Physical properties of samples

of fillers significantly reduces the ultimate stress. This question is out of the scope of the present paper which will focus on elastic simulations only.

3. Methods

95 The numerical simulations are performed with a massively parallel FFT-based solver, AMITEX [Ami]. In addition, multi-phase materials behaviors have been implemented in order to account for composite voxels (i.e. voxels crossed by at least one interface). Various homogenization rules are proposed : Voigt, Reuss and Laminate.

3.1. FFT algorithm

100 The FFT-base solver AMITEX [Ami] uses the basic FFT scheme [Moulinec and Suquet (1998)] derived from the introduction of a polarization term $\tau(x) = (c(x) - C_0) : \varepsilon(x)$, where c and C_0 are the local (heterogeneous) and reference (uniform) stiffness tensors respectively, and ε is the local strain tensor. For a given polarization field τ , the strain field is evaluated by computing the convolution of the Green operator: $\varepsilon(x) = -\Gamma_0 * \tau(x) + E$, with E being the average strain applied to the considered domain. This strain field is used to evaluate a new polarization and **thus, can be recalculated using the Green operator and so on until the field reaches the desired convergence criteria.** This defines the fix-point algorithm. In Fourier space, the convolution operation becomes a simple local tensorial product. The operator used in Amitex is a modified discrete Green operator as described in [Willot (2015)]. A convergence acceleration technique is applied to the FFT-based fixed-point algorithm. It corresponds to Andersons acceleration outlined by Chen [Chen et al. (2018)] **and can be applied to linear elasticity as well as complex non-linear constitutive behaviors.**

Finally, the coupled use of the modified Green operator and the convergence acceleration technique makes possible and quite efficient simulations with infinite mechanical contrasts.

3.2. Composite voxels geometrical definition

115 In classical FFT simulations (without composite voxels), the properties of each voxel are equal to the properties of the phase which is present at the voxel center. This allocation of properties is obvious when

the voxel consists of a single phase, but in the case of voxels crossed by an interface (i.e. voxels made of several phases), it consists of a rough approximation. That's why for complex microstructures, a very thin discretisation can be needed and thus involve long computation times. To mitigate this problem, the method of the composite voxels consists in evaluating the properties of a composite voxel from one of the homogenization rules presented in next section (3.3). Hence, as a first step, the composite voxels must be identified and characterized: their volume fractions of phases and the interface normal must be evaluated.

HGM are modelled by two concentric spheres. Evaluating the exact geometrical intersection between a sphere and a voxel is not straight forward and a simplified method is proposed to identify and characterize composite voxels Fig. 4. A voxel is considered composite if the circumscribed sphere of the voxel intersects one (or several) spheres. The volume fractions of each phase within the voxel are evaluated from the volume of intersections of the spheres. The interface normal is approximated by the direction relating both centers.

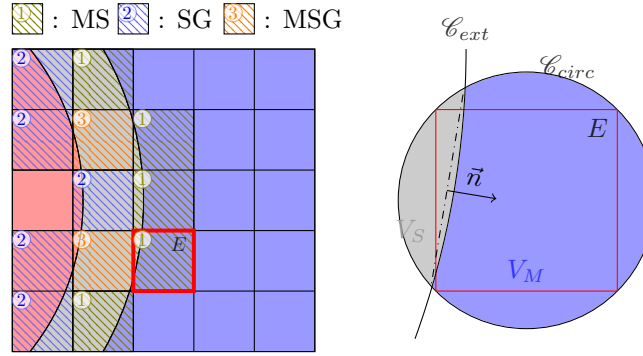


Figure 4: Composite voxels identification, volume fraction and normal vector approximation

We can then distinguish three types of composites voxels: two-phase voxels made of matrix and shell (MS) or made of shell and gas (SG) and three-phase voxels made of matrix, shell and gas (MSG). It can be noticed that for a small enough grid resolution, the three-phase voxels disappear.

In the case of random microstructures, two close microspheres can cross the same voxels and the definition of the composite voxel properties are done as follows. The volume fractions of the different phases are evaluated according to the procedure introduced above (Fig. 4). However, this procedure provides two normal vectors oriented from the voxel center towards each microspheres center. Considering that the voxel size is quite small compared to the sphere diameters, these vectors are almost collinear, so that the unique normal vector required for the laminate homogenization rule is approximated by the average normal vector, weighted by the glass contents : $n = f_1 n_1 - f_2 n_2$ with n_i the normal vectors of microsphere calculated as previously and f_i the glass volume fractions, from each microsphere, within the composite voxel.

Later on, resolution is defined as the ratio HGM thickness/voxel size, that represents the number of

voxels in the shell thickness of the microsphere.

140 3.3. Homogenization rules for composite voxels

Once characterized the composite voxels, an homogenization rule must be chosen to derive their effective properties. In AMITEX, three homogenization rules have been implemented: Voigt, Reuss and Laminate. These rules are used to derive the effective elastic tensor C from the N phases volume fractions f_i and elastic properties c_i .

145 The Voigt rule assumes an homogeneous strain over all the phases. It is an upper bound (stiff) for the homogenised elastic properties. The Reuss rule assumes an homogeneous stress over all the phases. It is a lower bound [Bornert et al. (2001)]. The corresponding effective stiffness tensors are given by :

$$C^{Voigt} = \sum_{i=1}^{Nphase} f_i c_i \quad (2)$$

$$C^{Reuss} = \left(\sum_{i=1}^{Nphase} f_i c_i^{-1} \right)^{-1} \quad (3)$$

In addition to these upper and lower bound, the laminate homogenization rule is proposed. It provides the exact solution for an infinite laminate material. In that case, stresses and strains are constant per phase. 150 Equilibrium and compatibility conditions are satisfied by the continuity of the out-of-plane stress (σ^{OP}) and of the in-plane strain (ε^P). The corresponding set of equations is given below, where $\bar{x} = \sum f_i x_i$:

$$\begin{cases} \sigma_i^{OP} = \overline{\sigma^{OP}} & i = 1..Nphases \\ \varepsilon_i^P = \overline{\varepsilon^P} & i = 1..Nphases \\ \sigma_i = c_i \varepsilon_i & i = 1..Nphases \end{cases} \quad (4)$$

Solving this set of equations leads to the definition of the Laminate homogenized stiffness tensor. In practice ε_i are the unknowns, equation 4.2 directly determines ε_i^P , and injecting 4.3 in 4.1 provides a 3xNphases linear system where ε_i^{OP} are unknowns.

155 4. Optimizing composite voxels

Once the composite voxels identified and characterized, the next questions are: first, to optimize the combination of homogenization rules (i.e. one homogenization rule, Voigt, Reuss or Laminate, per type of composite voxel, MS, SG and MSG), and second, to demonstrate the potential of FFT-based methods, equipped with composite voxels, to evaluate normal stresses at the HGM/matrix interface.

160 4.1. Optimization on the macroscopic response

The optimization of the homogenization rules combination is performed on a simple microstructure consisting of a single HGM with a volume fraction of 0.3 and a thickness/radius ratio of 0.1, representative of 3M-iM30K microspheres (see [subsec. 2.1](#)). Due to periodic boundary conditions, the virtual material has a simple cubic symmetry. PP is used as the reference matrix and in order to explore various possible thermoplastic matrices, 10 times stiffer and softer elastic properties are also considered. The corresponding Young moduli are 110, 1100 and 11000 MPa and the elastic contrast with respect to the glass Young modulus are respectively 630, 63 and 6.3. The loading is a uniaxial average stress tensor and the macroscopic response is the simulated average strain tensor. The quality of a simulation is estimated by the relative error on the average strain :

$$Err_{\bar{E}} = \frac{\|\bar{E} - \bar{E}^\infty\|_2}{\|\bar{E}^\infty\|_2} \quad (5)$$

170 With :

$$\|X\|_2 = \sqrt{X : X} = \sqrt{\sum_{i,j} X_{ij}^2} \quad (6)$$

For a given simulation, \bar{E} is the average strain tensor and \bar{E}^∞ is obtained from a simulation without composite voxels but with a high enough spatial resolution (shell thickness / voxel size of 6) to reach convergence (see black curves on [Fig. 5](#)).

175 It appears clearly that the convergence of the simulations without composite voxels ([Fig. 5](#) black curves) is more difficult when the matrix/shell contrast increases (i.e. when the matrix stiffness decreases). However, for the highest contrast ([Fig. 5-A](#), red and blue solid lines), the use of composite voxels and especially triple composite voxels, allows to obtain a precise estimate of the solution with less than one voxel in the glass shell (1% error is obtained for a shell thickness / voxel size of 0.7). In addition, for the three contrasts, there is always one combination of homogenization rules improving convergence.

180 From [Fig. 5](#) it appears clearly that: first, the Reuss homogenization rule (green curves) is not suitable for Shell/Gas composite voxels as the results are even worse than without composite voxels, and second the Laminate homogenization rule is the most appropriate for the Matrix/Shell composite voxels (compare A-D-G graphs with B-E-H and C-F-I, without considering green curves). In that case, graphs on [Fig. 5](#) A-D-G, looking at spatial resolutions lower than 1.73 (i.e. if a is the voxel size, $\sqrt{3}a \approx 1.73a$ is the largest distance between opposite corners, and if this value is smaller than the shell thickness, triple composites cannot exist) for which triple composites (MSG) exist, the Reuss homogenization rule is not suitable for

triple composites (see dash-dot lines). Among the remaining combinations, the full laminate combination (solid red lines) is in overall well appropriate for the three elastic contrasts. Besides, in our specific case of interest (Fig. 5-D for $E_{mat} = 1100$ MPa), the solution (MS : Laminate, SG : Voigt, MSG : Laminate) is the best choice. These combinations will be our two choices in the following. For an alternate display, readers are invited to consult appendix A where results for this specific case are gathered in histogram plots.

It is worth noting that, while the full laminate combination appears quite natural, it gives very satisfying results but not the best results. The best results are obtained when using the Voigt approximation for the SG composite voxels. If the explanation of this counterintuitive result is yet unclear, it may be related to the infinite elastic contrast observed in SG composites voxels. Actually, such an infinite contrast combined with the laminate homogenization rule induces an infinitely anisotropic behavior, which is suspected to be ill suited to our FFT-based simulations. This point should be clarified in the future. However, as a practical conclusion of this discussion, in the presence of infinite contrasts, readers are invited to consider isotropic homogenization rules such as Voigt or Reuss, in addition to the Laminate model, leading to infinite anisotropy.

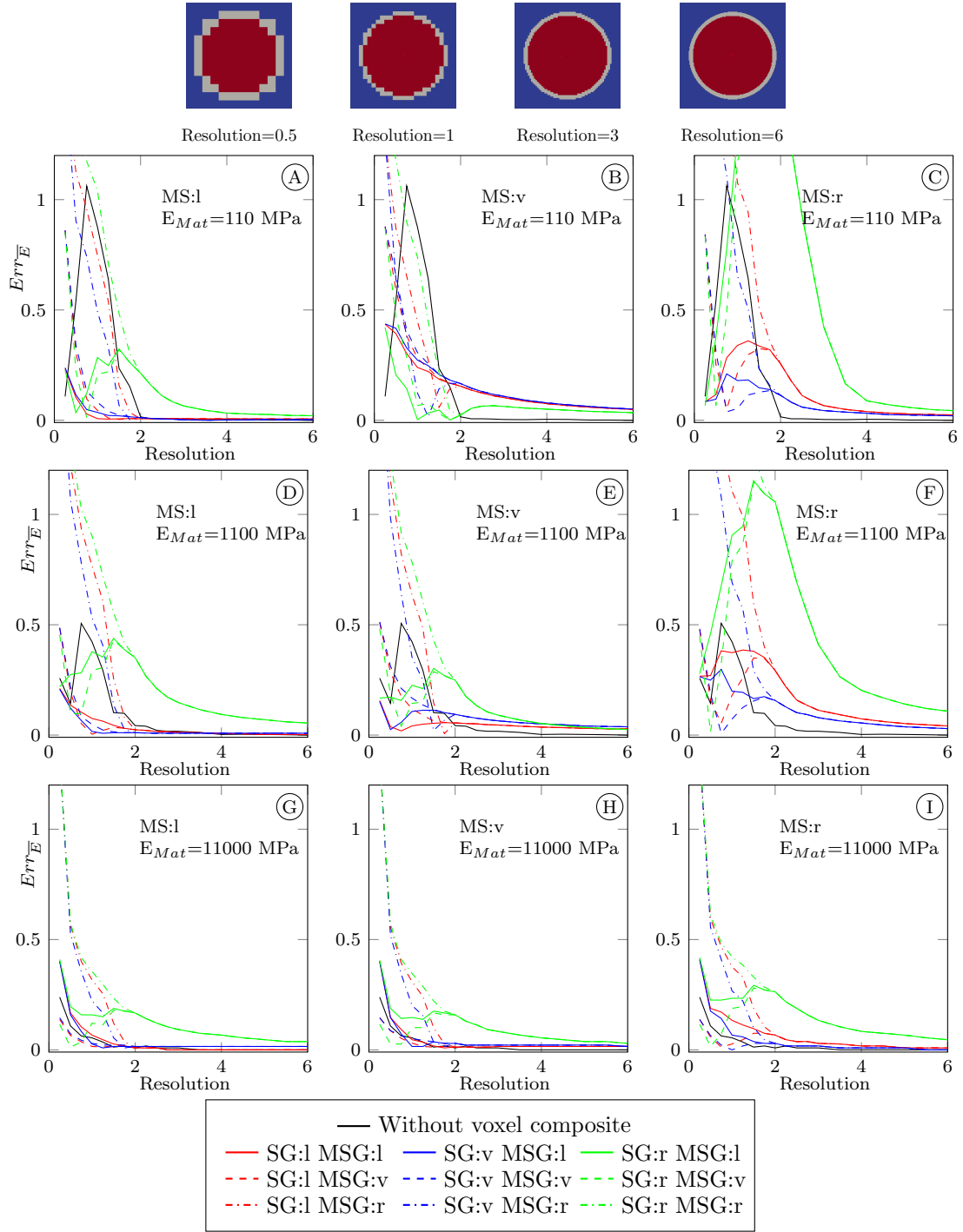


Figure 5: Relative error as a function of the resolution for all combinations of composite voxels homogenization rules and for several contrasts ($E_{mat}=110, 1100, 11000$ MPa - $fv=0.3$, $E_{shell}=69000$ MPa). Notations : MS : Matrix/Shell, SG : Shell/Gas, MSG : Matrix/Shell/Gas for the composite voxels, and, l : Laminate, v : Voigt, r : Reuss for the homogenization rules.

4.2. Optimization on the evaluation of normal stresses at interfaces

Evaluating normal stresses at HGM/matrix interfaces is of interest to discuss potential debonding mechanism [Gilabert et al. (2015)]. However, even using Finite Elements with a conforming mesh, their evaluation is not straightforward because stresses are defined at Gauss points in the volume of elements and not at the interface between elements. Various methodologies are proposed to this end. For example, Diard introduces additional Gauss points at the surface in order to extrapolate the stress [Diard et al. (2005)] while Shawish introduces additional cohesive elements, with an ad-hoc stiffness (high enough to reduce the spurious additional softening, and not too high to avoid numerical issues) [El Shawish et al. (2013)]. At first glance, FFT-based methods, using a regular mesh, seem to be ill-suited for this application. After introducing the methodology, we will demonstrate that using composite voxels in the simulation allows to obtain good quality results. The test case is the same as in section 4.1 with the elastic properties of PP for the matrix.

The post-treatment used to evaluate stresses at HGM/matrix interface is rather simple: the stress field is projected on a surface mesh of the interface. A Marching cube algorithm, used for detecting iso-surfaces of a 3D scalar function defined on a regular grid, provides the triangle mesh of the interface. In practice, the isosurface function of matlab[®] is applied to a scalar field representing the distance to the HGM center and the regular grid is defined on the unit-cell, with a voxel size equal to the smaller one used for simulations. In the following, the surface triangle mesh used for evaluating normal stresses is deduced from a grid of 475^3 voxels.

For each triangle element i , the surface dS_i , the normal vector n_i and the voxel j containing the triangle barycenter can be determined to evaluate the normal stress as $\sigma_n^i = n_i \sigma^j n_i$ so that a constant per triangle field can be drawn (see Fig. 6). The error indicator defined below assesses the quality of the result as a function of the resolution :

$$Err_{\sigma_n} = \frac{\sqrt{\int_S (\sigma_n - \sigma_n^{i\infty})^2 dS}}{\sqrt{\int_S \sigma_n^{i\infty 2} dS}} \simeq \frac{\sqrt{\sum_{i=1}^{N_{triangles}} (\sigma_n^i - \sigma_n^{i\infty})^2 \delta S^i}}{\sqrt{\sum_{i=1}^{N_{triangles}} \sigma_n^{i\infty 2} \delta S^i}} \quad (7)$$

Where $\sigma_n^{i\infty}$ stands for the converged normal stress field, evaluated with a spatial resolution of 20 (i.e. shell thickness/voxel size) corresponding to a grid of 475^3 voxels, using the homogenization rules combination for the composite voxels optimized in the previous section for that specific case (MS: Laminate, SG : Voigt, MSG : Laminate).

It is clear on Fig. 6, whether on the noisy fields or on the high value of the error indicator that, if not equipped with composite voxels, the FFT-based method is not able to evaluate normal stresses at HGM/matrix interfaces. On the other hand, with composite voxels and a spatial resolution higher than

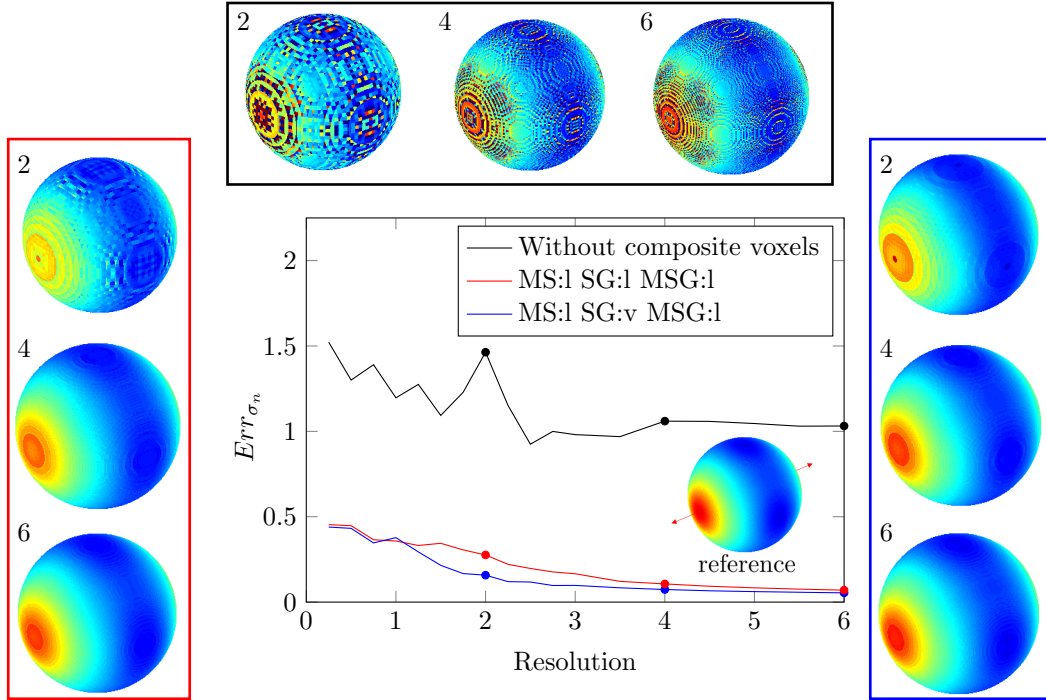


Figure 6: Normal stress fields evaluated from simulations without composite voxels (black frame), with the full Laminate combination (red frame) and with the combination (MS : Laminate, SG : Voigt, MSG : Laminate) (blue frame), for spatial resolutions 2, 4 and 6. The corresponding error indicators (Eq. 7) are plotted as a function of the spatial resolution.

2, the normal stress fields appear very smooth. For resolution 2, the combination (MS : Laminate, SG : Voigt, MSG : Laminate) provides a smoother field compared to the full laminate combination. It confirms at a local scale that, for this set of material properties, the Voigt homogenization rule for the Shell/Gas composite voxels produces better results than the Laminate rule, and justifying a posteriori, this choice as the reference in the error indicator (Eq. 7).

To conclude, the resolution chosen for the evaluation of interface normal stresses in the next section is 3 and the corresponding homogenization rules combination is (MS: Laminate, SG : Voigt, no triple voxel for resolution 3).

4.3. Discussion on the convergence of the FFT-based solver

The previous sections analyze the effect of composite voxels on the numerical solutions provided by the FFT-based solver, whether the macroscopic behavior or the local stresses at matrix-shell interface. Here, the effect of composite voxels is analyzed on the convergence of the iterative FFT-based algorithm (i.e. a fixed-point algorithm combined with a convergence acceleration technique). The analysis is limited to the

reference PP matrix (Tab. 2) and the Lamé coefficients of the reference medium, used for the FFT-based solver, are given by the rule $(\min(\cdot)+\max(\cdot))/2$ applied to Lamé coefficients over the whole unit-cell. Fig. 7 gathers in histogram plots, for three resolutions (0.75, 1.5 and 2), the number of iterations at convergence as a function of the homogenization rules combinations. These increasing resolutions are associated to a decreasing number of 3-phase composite voxels involved to describe the shell thickness; up to a complete loss for resolution 2. As a result, the effect of the homogenization rule for 3-phase voxels (MSG) is null for resolution 2 and increases when decreasing the resolution.

For the three resolutions, and more evidently for resolution 2, the homogenization rule used for shell-gas composite voxels has an important effect: the best convergence is obtained with Voigt homogenization rule and the worst with Laminate. Our interpretation is that, with null properties for the gas, the Voigt rule provides a smooth transition zone, of one voxel thickness, from gas voxels to shell voxels. On the other hand, the Reuss rule replaces composite voxels by gas voxels, reducing de facto the thickness of the shell. Finally, the infinitely anisotropic behavior provided by the Laminate rule for SG composite voxels proves to be ill suited from the convergence point of view. This point is in agreement with the conclusion proposed in subsec. 4.1 deduced from the analysis of the numerical response.

To conclude, for resolutions without triple composite voxels (>1.73), the choice deduced from an analysis of the numerical response is also the best choice for the convergence of the FFT-based solver. For the lowest resolution (i.e. 0.75), the optimal results for the convergence are obtained with the Voigt rule for triple composite voxels, which is also consistent with the macroscopic results observed on Fig. 5-D.

5. Applications

Once optimized the homogenization rules combination and the resolution (sec. 4), the behavior of simple periodic microstructures is first analyzed. Then, random microstructures are considered in order to simulate both the macroscopic behavior and the stresses at HGM/matrix interfaces of the composite material under investigation. In this section, the material properties of the three phases (void, matrix and shell) are listed in Tab. 1.

5.1. Periodic microstructures

Simulations were performed on three periodic microstructures, with cubic (C), body centered cubic (BCC) and face centered cubic (FCC) symmetries, and with a common microsphere volume fraction of 0.3. The microspheres are the same as used in subsec. 4.1 with a thickness/radius ratio of 0.1, representative of 3M-iM30K microspheres, in agreement with Eq. 1. From sec. 4, the resolution used for the simulations is 3 and the homogenization rule combination is (MS : Laminate, SG : Voigt, no triple voxels for such this

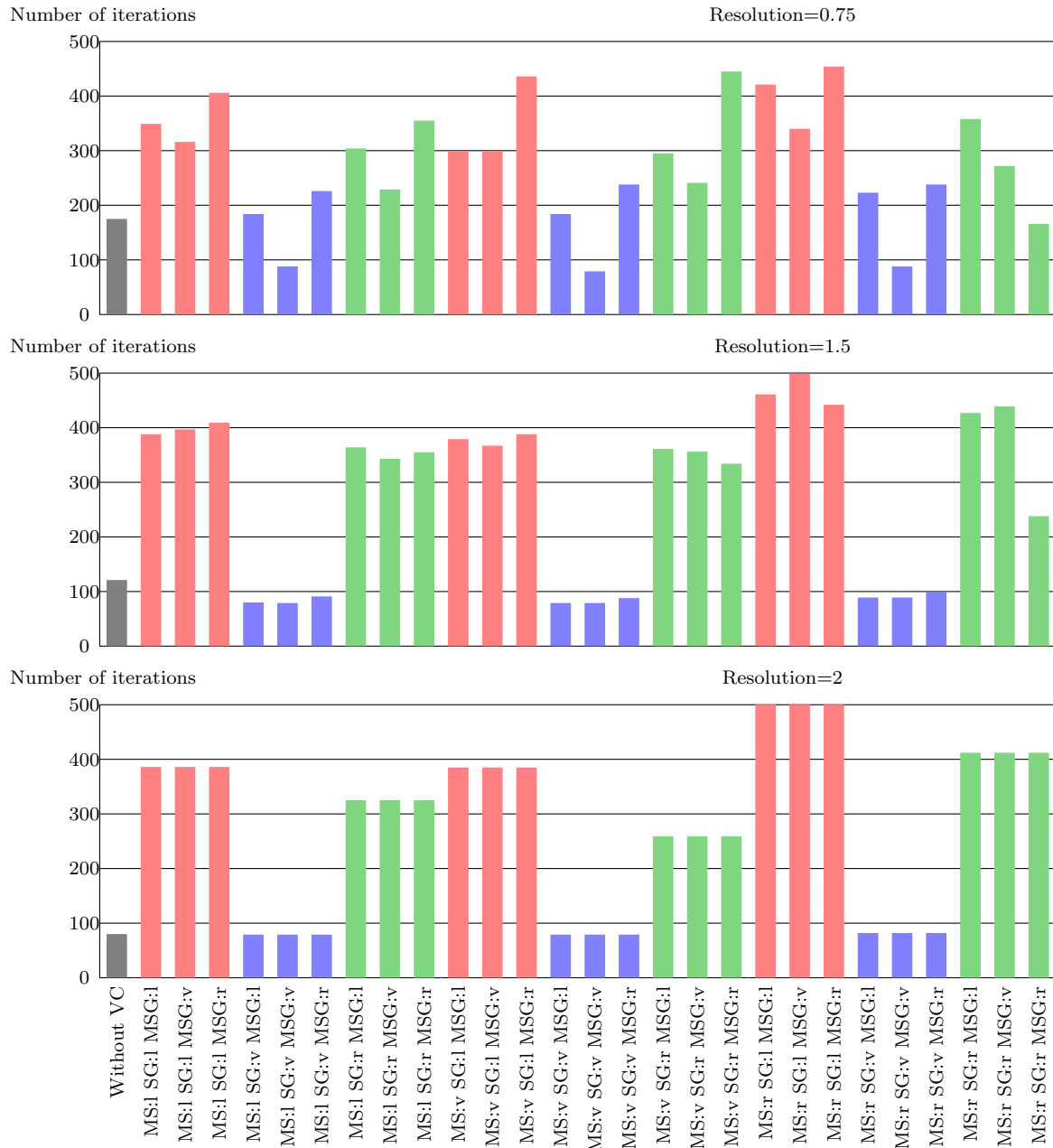


Figure 7: Histogram plot of number of iterations as a fonction of all combinations of composite voxels homogenization rules for the resolution of 0.75, 1.5 and 2 and for the reference matrix properties (i.e. shell/matrix elastic contrast = 63).

275 resolution). Six independent loadings (three uniaxial tensile tests and three shear tests) were applied in order to evaluate all the components of the effective (i.e. homogenized) stiffness tensor. Fig. 8 draws the effective Youngs modulus anisotropic surface for each microstructure. For the sake of comparison, the so-called (n+1) phases homogenization model [Herve and Zaoui (1993)] was also used. This model is not able to account for

an anisotropic distribution of spheres and the homogenized behavior is isotropic. Consequently, the effective
280 Youngs modulus surface is a sphere (radius 1778 MPa) and, for the clarity of Fig. 8, it is rather represented
by a simple circle.

Qualitatively, Fig. 8 reveals that the anisotropy of the effective behavior is quite different between the
C microstructure and the BCC and FCC ones, while these two microstructures (BCC and FCC) exhibit
a similar anisotropy. Besides, the "(N+1) phases" model provides a satisfying isotropic estimate as, for
285 the three symmetries; the sphere (represented by the blue circle) is neither inscribed nor circumscribed by
the anisotropic surfaces. The anisotropy of cubic-symmetry elasticity is quantitatively characterized by the
Zener ratio ($A = 2C_{44}/(C_{11} - C_{12})$, where the three C_{ij} denote the three independent Voigt elastic stiffness
coefficients). For isotropic materials, $A = 1$ [Ledbetter and Migliori (2006)]. The Zener ratios of the studied
structures are: $A_C = 0.885$, $A_{BCC} = 1.044$ and $A_{FCC} = 1.035$. The Zener ratio can be related to the
290 coordination number (i.e. number of first neighbors) for each structures (6, 8 and 12 for C, BCC and FCC):
the higher the coordination number, the lower the anisotropy.

Fig. 8 also draws the distributions of normal stresses at HGM/matrix interfaces for a uniaxial tensile
stress loading (1 MPa). For that specific loading, the normal stresses at interface are the highest for the
cubic symmetry and the lowest for the FCC symmetry.

295 In the context of designing architected periodic materials [Wang et al. (2011); Yu et al. (2018)] for
a given application (i.e. for a given load), it can be observed that the symmetry of the periodic cell can
be optimized with respect to the effective behavior, but also to the stresses at HGM/matrix interfaces,
especially if damage initiates at these interfaces.

5.2. Random microstructures

300 In order to perform simulations on materials with a microstructure close to the experimental one, a
random microstructure generator was set up. At first, a desired number of diameter is randomly drawn
from the distribution characterized experimentally (Fig. 1). Then, Eq. 1, deduced from diameters and
thickness measurements, gives the shell thickness of each microsphere. Finally, the size of the simulation
box is adjusted to the desired volume fraction and the microspheres are scattered in this simulation box
305 according to a random sequential adsorption model [Meakin and Jullien (1992)]. This model generates non-
overlapping microspheres homogeneously distributed in space (no clustering) consistently with tomographic
observations (Fig. 2). With the studied diameter distribution, this model can easily reach volume fractions
greater than 50%. Note that the RSA model is used with periodic boundary conditions in order to generate
periodic microstructures, better suited with the periodic boundary conditions applied in FFT-based sim-
310 ulations. **Finally, it must be emphasized that the RSA is applied without imposing any minimal distance**

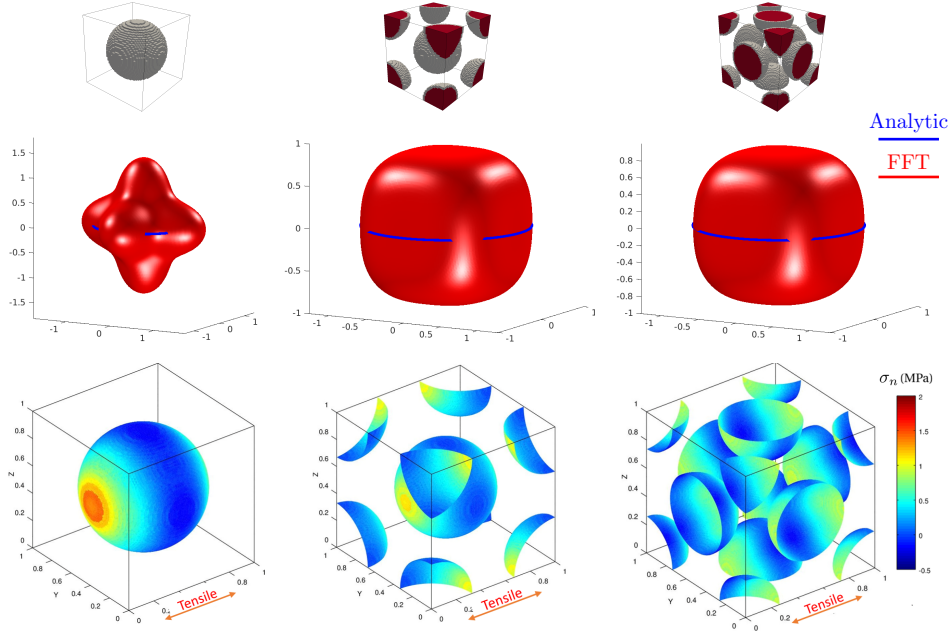


Figure 8: Young's modulus (MPa) in x-y plane for three periodic microstructures (left : cubic, middle : centered cubic, and right : face-centered cubic) and, below, the equivalent normal stress at the interfaces for a uniaxial tensile stress (1 MPa) ($f_v=0.3$, $E_{shell}=69000$ MPa, $E_{mat}=1100$ MPa, composite voxels type MS=1 SG=v MSG=1, resolution=3)

between spheres (repulsion distance). In FE simulations, such a minimal distance is often set artificially to avoid numerical issues. In our simulations, quasi contact between spheres are approximated by three-phase composite voxels (see subsec. 3.2) so that there is no strong numerical issue requiring to impose a minimal distance. In addition, without any experimental evidence and/or measurement of such a minimal distance on the real microstructure, we have assumed that the manufacturing process does not impose it.

315

Before evaluating the effect of the microsphere volume fraction on the effective isotropic elastic properties, the size of the representative unit-cell must be determined. For that purpose, uniaxial tensile tests are applied to unit-cells of different sizes (i.e. different number of spheres) and for each size, 10 samples are randomly generated and simulated. For this study, the most penalizing case, corresponding to the highest volume fraction (i.e. 50%), is considered. The spatial resolution sensitivity is also studied in that context of random microstructures. For each tensile test simulation, an average Young modulus (E) and two Poisson coefficients (ν_{12} and ν_{13}) can be evaluated as follows :

320

$$E = \frac{\bar{\sigma}_{11}}{\bar{\epsilon}_{11}} \quad ; \quad \nu_{12} = \frac{\bar{\epsilon}_{22}}{\bar{\epsilon}_{11}} \quad ; \quad \nu_{13} = \frac{\bar{\epsilon}_{33}}{\bar{\epsilon}_{11}} \quad (8)$$

With $\bar{\sigma}_{11}$ and $\bar{\epsilon}_{11}$ the average stress and strain in the direction of traction and $\bar{\epsilon}_{22}$ and $\bar{\epsilon}_{33}$ the average

strain in the transverse directions. Fig. 9 gathers all the results. The mean Young modulus decreases
 325 with the size of the unit-cell until reaching convergence. For 256 spheres, this quantity is converged (no
 difference with 64 spheres) and the relative standard deviation is less than 1.5% : as similar conclusions can
 be drawn from the Poisson coefficients evolutions, this size is then considered as representative and kept for
 further simulations. Regarding resolution, convergence is reached for 1.5. This result confirms that, thanks
 to composite voxels, a resolution of 1.5 (i.e. ratio shell thickness/voxel size) is sufficient for an accurate
 330 estimate of the macroscopic elastic behavior.

Fig. 10 draws the evolution of the Young modulus as a function of the microspheres content in the
 range of [0%-50%], obtained from uniaxial stress (1 MPa) simulations performed on 256 spheres unit-cell
 with a spatial resolution of 1.5. Two strain fields reported on Fig. 10, for 0.1 and 0.5 contents, provide a
 visualization of the microstructures and an indication of the quality (smoothness) of the simulated fields.
 335 Comparison with experimental results reveals a very nice agreement up to 30%. For higher values, a
 small discrepancy appears but remains reasonable (less than 10%). Note that, in the light of the slight
 irregularity of the experimental curve, artefacts coming from the Young modulus measurement and/or the
 manufacturing process, are also suspected to explain this discrepancy. From the modelling point of view,
 it must be emphasized that, compared to FFT simulations and experimental results, the (N+1) phases
 analytical model is too stiff especially when the HGM volume fraction increases. From a practical point of
 view, it is worth noting that adding a content of 50% HGM increases the stiffness by a factor of almost two
 340 (from 1100MPa to 2077MPa).

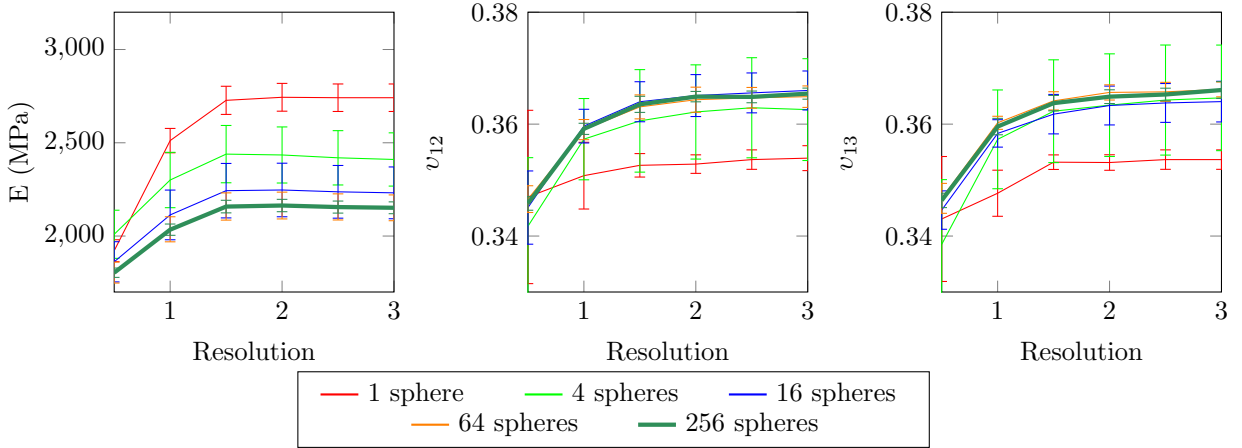


Figure 9: Convergence study of the mean (over 10 samples) Young modulus and Poisson's coefficients according to the number of spheres and the resolution. Error bar show standard deviation on the different samples. ($fv=0.5$, $E_{shell}=69000$ MPa, $E_{mat}=1100$ MPa, Composite voxels type MS=1 SG=v MSG=1)

Finally, in order to evaluate and discuss the normal stresses at HGM/matrix interfaces, the same

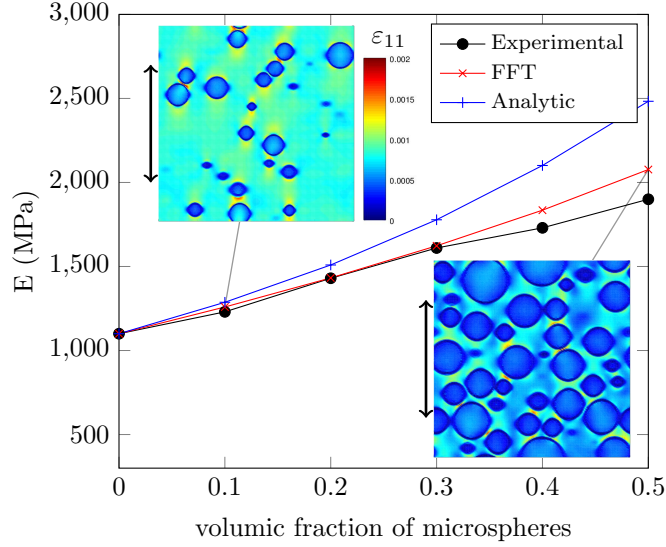


Figure 10: Evolution of the effective Young modulus with respect to microspheres volume fraction and strain fields in a longitudinal slice for volume fractions 0.1 and 0.5 obtained from FFT computations (resolution=1.5, Nb sphere=256, E_{shell} =69000 MPa, E_{mat} =1100 MPa, Composite voxels type MS=1 SG=v MSG=1)

simulations (256 spheres, uniaxial stress 1 MPa, volume fractions 0.1, 0.2, 0.3, 0.4, 0.5) are performed but
 345 now with a spatial resolution of 3 (i.e. 751^3 and 413^3 voxels for 0.1 and 0.5 contents, respectively). For every microspheres, the normal stress fields at HGM/matrix interfaces are evaluated according to the method detailed in [subsec. 4.2](#). **Prior to further statistical analysis, the question of a possible artefact, relating the interface normal stress to the glass volume content within Matrix-Shell composite voxels, is alleviated in [appendix B](#).** Then, the fields evaluated over the 256 spheres are gathered onto a reference sphere through two
 350 statistical quantities: the average normal stress, $\langle \sigma_n \rangle$, and the relative standard deviation of σ_n , $RSD(\sigma_n)$. [Fig. 11](#) draws these quantities on the reference sphere, and on one of its equators using a polar representation. Before describing these plots, it is worth noting that the spatial average over the reference sphere of $\langle \sigma_n \rangle$ appears to be almost insensitive with respect to the HGM volume fraction (0.37 MPa and 0.36 MPa for 0.1 and 0.5 contents, respectively). Regarding the distribution of $\langle \sigma_n \rangle$, the axisymmetry of the field over
 355 the reference sphere together with the smoothness of the polar curves, reveals at least qualitatively that the sphere distribution is isotropic and the number of spheres (256) is sufficient for that purpose. Actually, the same representations made for single spheres are clearly not axisymmetric. The effect to the HGM volume fraction is not important but not negligible : $\langle \sigma_n \rangle$ increases in the tensile test direction and decreases in the transverse direction when decreasing the HGM content. A 13% decrease is observed in the tensile direction
 360 between 0.1 and 0.5. It is interesting to compare the results obtained on $\langle \sigma_n \rangle$ with the normal stress around a sphere, assuming a uniform stress field equal to the average applied stress (plotted in green, [Fig. 11](#)). It

can be noted that the mean normal stress field tends towards a uniform stress assumption when increasing the microsphere volume content. Regarding the relative standard deviation of σ_n , the axisymmetry of the field is less pronounced and the polar curve exhibit fluctuations, revealing that the number of spheres (256) is not sufficient to provide precise quantitative results but enough to draw sound qualitative trends. A few large peaks, observed on the fields, are associated to quasi contacts between spheres. They could have been avoided by using a repulsion distance in the random sequential adsorption, as often proposed in order to avoid numerical issues in FE simulations [Segurado and Llorca (2002); Gilormini et al. (2017); Brown et al. (2018); De Francqueville et al. (2019)]. Finally, despite of these fluctuations, it is clear that the Relative Standard Deviation of σ_n increases significantly with the HGM content, especially in the tensile test direction (+40% between 0.1 to 0.5 contents). To conclude this analysis, it is demonstrated here that if the level of normal stresses decreases in average when increasing the HGM content (-13% in the axial stress direction), the relative standard deviation of σ_n increases in a larger proportion (+40% in the axial stress direction). Hence, if the HGM/matrix interface decohesion is confirmed being a significant damage mechanism, increasing the HGM volume fraction should promote this mechanism.

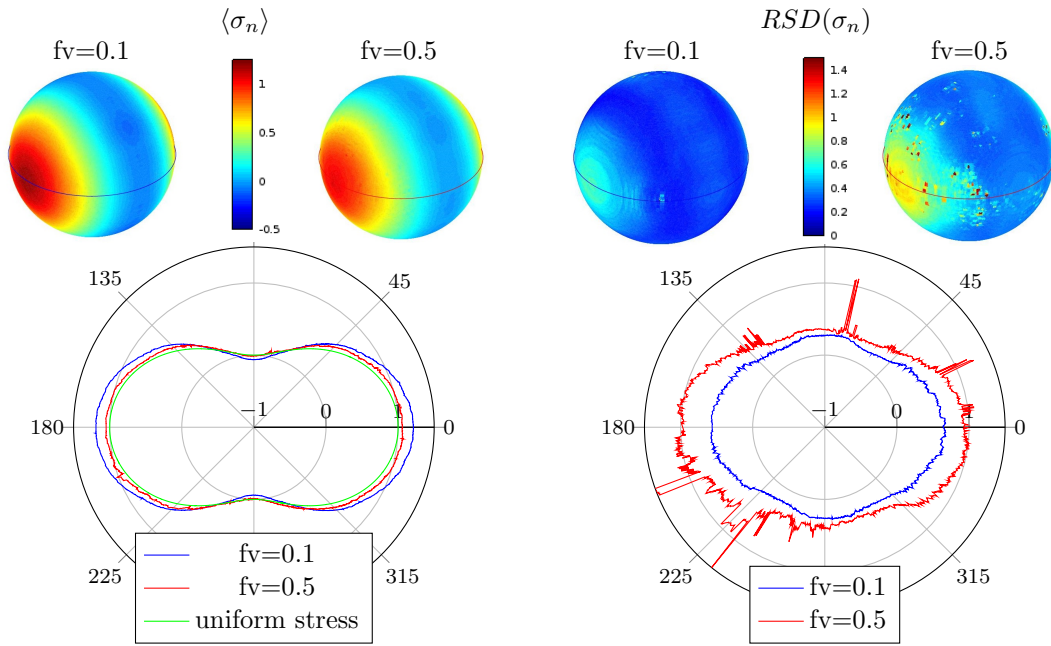


Figure 11: Average (left) and Relative Standard Deviation (right) of the normal stress at HGM/matrix interface evaluated on 256 spheres and gathered on a reference sphere. Simulations are performed for a uniaxial stress loading (1 MPa), with elastic properties reported in table 1, a resolution of 3 and the following composite voxels types : MS=1, SG=v and no triple voxels for that resolution. On the polar representation, corresponding to the equator drawn on the spheres, grey circles correspond to 0MPa and 1MPa (the applied uniaxial stress).

6. Conclusions and future prospects

Since the last generation of Hollow Glass Microspheres (HGM), the development of HGM-thermoplastic composites is in progress in order to increase the stiffness of the material while reducing the density. Together with the development of a manufacturing process of polypropylene HGM composites, a numerical approach is in progress to predict their macroscopic mechanical behavior but also the local stresses arising within the composites. Instead of using a standard Finite Element approach, one purpose of the paper is to demonstrate the capabilities of FFT-based solvers for this specific application, at first for elastic behaviors. The second purpose concerns the application and validation of the method with respect to an in-house manufactured material characterized experimentally.

The use of composite voxels is proposed and optimized in order to overcome two main issues: the thin thickness of HGM together with a uniform grid-refinement and the evaluation of normal stresses at HGM/matrix interface with a non-adapted, voxel-based mesh. The macroscopic behavior can be evaluated precisely with a spatial resolution as low as 0.7 (voxel in the HGM thickness) and a resolution of 3 is required for evaluating normal stresses at HGM/matrix interface. In addition, the paper also demonstrates that evaluating interface normal stresses directly with an FFT-based solver is not possible without using composite voxels.

The numerical method has been applied and compared to experimental results obtained on in-house manufactured HGM-polypropylene composites. Realistic random microstructures were generated from measurements (sphere diameters and thickness) and observations (homogeneous distribution of spheres verified by X-ray tomography). The Young moduli evaluated experimentally for different HGM volume fraction (0.1, 0.2, 0.3, 0.4 and 0.5) compares very well to the prediction of the model, whereas the so-called "N+1 phases" analytical model is too stiff. Finally, in view of a potential interfacial debonding mechanism (to be confirmed by an experimental study in progress), a statistical analysis of the interface normal stress distribution is proposed as a function of the HGM content, for a given uniaxial stress loading. In average, the normal stress in the tensile direction slightly decreases (-13%) when increasing the content from 0.1 to 0.5, while, on the other hand, its Relative Standard Deviation increases significantly (+40%).

Now alleviated the issues associated to the application of FFT-based solvers to HGM composites, the next step will be to introduce the non-linear behavior of the matrix and the potential damage mechanisms such as interfacial debonding. Finally, if all the elastic simulations presented in the paper were performed on a single computer, FFT-based solvers can be efficiently parallelized through distributed memory implementations (as proposed in the code AMITEX [Ami]) which can be of a major interest when dealing with non-linear constitutive behaviors.

Appendix A

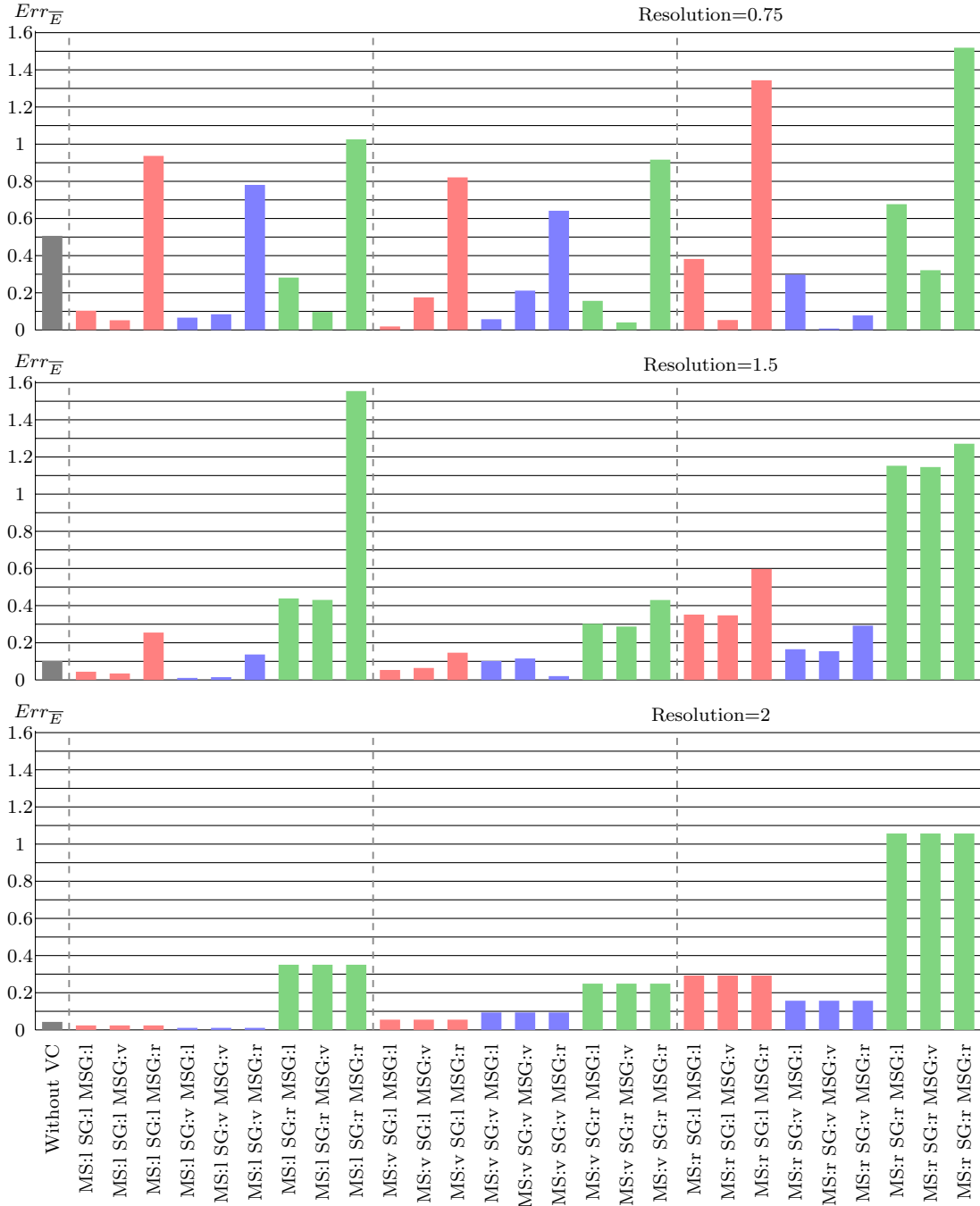


Figure 12: Histogram plot of relative error as a function of all combinations of composite voxels homogenization rules for the resolution of 0.75, 1.5 and 2 and for the reference matrix properties (i.e. shell/matrix elastic contrast = 63).

Appendix B

410 This appendix investigates the question of a possible artifact that would correlate the surface normal stresses (at Matrix-Shell interface) to the glass volume content, suspecting higher stresses with higher glass content. Figure 12 and 13, plot for every composite voxels the surface stress as a function of its glass content. It is clear that such a correlation is not observed. In addition, arbitrarily chosen microspheres are extracted to display, for the Matrix-Shell composite voxels, the glass content and the surface normal stresses. While
415 the glass content looks random, the distribution of surface stresses is rather smooth and not correlated to the glass content.

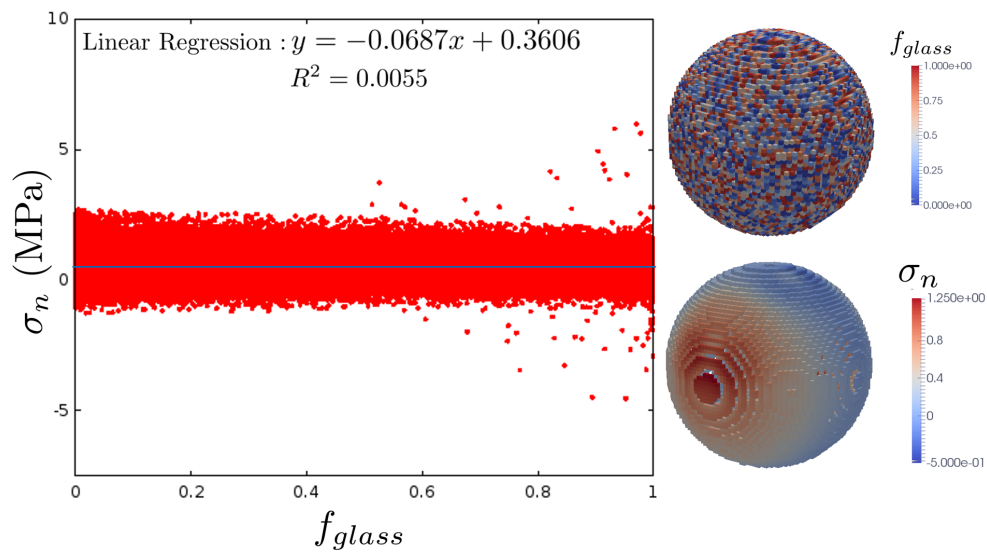


Figure 13: The normal stresses at HGM/matrix interfaces as a function of the glass volume content on every composite voxels evaluated on a microstructure with 256 spheres and HGM volume fraction of 0.1. The top sphere represents the distribution of the glass volume content in the composite voxels of one HGM (chosen arbitrarily), and at the bottom, the normal stress from the same microsphere.

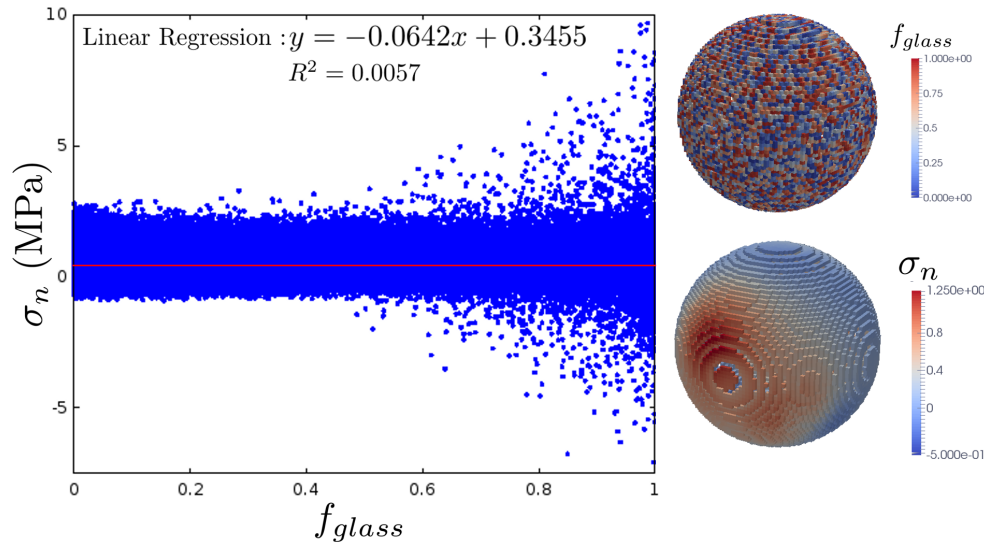


Figure 14: The normal stresses at HGM/matrix interfaces as a function of the glass volume content on every composite voxels evaluated on a microstructure with 256 spheres and HGM volume fraction of 0.5. The top sphere represents the distribution of the glass volume content in the composite voxels of one HGM (chosen arbitrarily), and at the bottom, the normal stress from the same microsphere.

References

- Amitex. URL <http://www.maisondelasimulation.fr/projects/amtex/html/index.html>.
- L. Bardella, F. Malanca, P. Ponzio, A. Panteghini, and M. Porfiri. A micromechanical model for quasi-brittle compressive failure of glass-microballoons/thermoset-matrix syntactic foams. *Journal of the European Ceramic Society*, 34(11):2605–2616, 2014.
- M. Bornert, T. Bretheau, and P. Gilormini. Homogénéisation en mécanique des matériaux. *Hermes Science Europe, Stanmore, UK*, 2001.
- J. Brown, J. Carroll, B. Huddleston, Z. Casias, and K. Long. A multiscale study of damage in elastomeric syntactic foams. *Journal of materials science*, 53(14):10479–10498, 2018.
- H. Çelebi. Thermal conductivity and tensile properties of hollow glass microsphere/polypropylene composites. *Anadolu Üniversitesi Bilim Ve Teknoloji Dergisi A-Uygulamalı Bilimler ve Mühendislik*, 18(3):746–753, 2017.
- Y. Chen, L. Gélébart, C. Chateau, M. Bornert, C. Sauder, and A. King. Analysis of the damage initiation in a sic/sic composite tube from a direct comparison between large-scale numerical simulation and synchrotron x-ray micro-computed tomography. *International Journal of Solids and Structures*, 2018.
- Y. Chen, D. Vasiukov, L. Gélébart, and C. H. Park. A fft solver for variational phase-field modeling of brittle fracture. *Computer Methods in Applied Mechanics and Engineering*, 349:167–190, 2019.
- Y. J. Cho, Y. Kang, Y. C. Lee, Y. Park, and W. Lee. Influence of partially debonded interface on elasticity of syntactic foam: A numerical study. *Materials*, 10(8):911, 2017.
- F. De Francqueville, P. Gilormini, and J. Diani. Representative volume elements for the simulation of isotropic composites highly filled with monosized spheres. *International Journal of Solids and Structures*, 158:277–286, 2019.
- O. Diard, S. Leclercq, G. Rousselier, and G. Cailletaud. Evaluation of finite element based analysis of 3d multicrystalline aggregates plasticity: Application to crystal plasticity model identification and the study of stress and strain fields near grain boundaries. *International Journal of Plasticity*, 21(4):691–722, 2005.

- S. El Shawish, L. Cizelj, and I. Simonovski. Modeling grain boundaries in polycrystals using cohesive elements: qualitative and quantitative analysis. *Nuclear Engineering and Design*, 261:371–381, 2013.
- L. Gélébart and F. Ouaki. Filtering material properties to improve fft-based methods for numerical homogenization. *Journal of Computational Physics*, 294:90–95, 2015.
- F. Gilabert, D. Garoz, and W. Van Paepegem. Stress concentrations and bonding strength in encapsulation-based self-healing materials. *Materials & Design*, 67:28–41, 2015.
- P. Gilormini, P.-A. Toulemonde, J. Diani, and A. Gardere. Stress-strain response and volume change of a highly filled rubbery composite: experimental measurements and numerical simulations. *Mechanics of Materials*, 111:57–65, 2017.
- N. Gupta, S. E. Zeltmann, V. C. Shunmugasamy, and D. Pinisetty. Applications of polymer matrix syntactic foams. *Jom*, 66(2):245–254, 2014.
- E. Herve and A. Zaoui. N-layered inclusion-based micromechanical modelling. *International Journal of Engineering Science*, 31(1):1–10, 1993.
- M. Hojo, M. Mizuno, T. Hobbiebrunken, T. Adachi, M. Tanaka, and S. K. Ha. Effect of fiber array irregularities on microscopic interfacial normal stress states of transversely loaded ud-cfrp from viewpoint of failure initiation. *Composites Science and Technology*, 69(11-12):1726–1734, 2009.
- J. Huang and L. Gibson. Elastic moduli of a composite of hollow spheres in a matrix. *Journal of the Mechanics and Physics of Solids*, 41(1):55–75, 1993.
- M. Kabel, D. Merkert, and M. Schneider. Use of composite voxels in fft-based homogenization. *Computer Methods in Applied Mechanics and Engineering*, 294:168–188, 2015.
- M. Kabel, A. Fink, and M. Schneider. The composite voxel technique for inelastic problems. *Computer Methods in Applied Mechanics and Engineering*, 322:396–418, 2017.
- H. Ledbetter and A. Migliori. A general elastic-anisotropy measure. *Journal of applied physics*, 100(6):063516, 2006.
- J. Liang and F. Li. Simulation of heat transfer in hollow-glass-bead-filled polypropylene composites by finite element method. *Polymer Testing*, 26(3):419–424, 2007.
- J.-Z. Liang. Estimation of thermal conductivity for polypropylene/hollow glass bead composites. *Composites Part B: Engineering*, 56:431–434, 2014.
- C. Mareau and C. Robert. Different composite voxel methods for the numerical homogenization of heterogeneous inelastic materials with fft-based techniques. *Mechanics of Materials*, 105:157–165, 2017.
- P. R. Marur. Effective elastic moduli of syntactic foams. *Materials Letters*, 59(14-15):1954–1957, 2005.
- P. R. Marur. Influence of imperfect interface on the elastic moduli of syntactic foams. *Computational Materials Science*, 46(2):327–332, 2009.
- P. R. Marur. Numerical estimation of effective elastic moduli of syntactic foams. *Finite Elements in Analysis and Design*, 46(11):1001–1007, 2010.
- C. McCarthy and T. Vaughan. Micromechanical failure analysis of advanced composite materials. In *Numerical Modelling of Failure in Advanced Composite Materials*, pages 379–409. Elsevier, 2015.
- P. Meakin and R. Jullien. Random sequential adsorption of spheres of different sizes. *Physica A: Statistical Mechanics and its Applications*, 187(3-4):475–488, 1992.
- Q. Meng and Z. Wang. Prediction of interfacial strength and failure mechanisms in particle-reinforced metal-matrix composites based on a micromechanical model. *Engineering Fracture Mechanics*, 142:170–183, 2015.
- H. Moulinec and P. Suquet. A numerical method for computing the overall response of nonlinear composites with complex microstructure. *Computer methods in applied mechanics and engineering*, 157(1-2):69–94, 1998.
- L. Nielsen. Elastic modulus of syntactic foams. *Journal of Polymer Science: Polymer Physics Edition*, 22(3):535–535, 1984.
- T. Okabe, M. Nishikawa, and H. Toyoshima. A periodic unit-cell simulation of fiber arrangement dependence on the transverse

- tensile failure in unidirectional carbon fiber reinforced composites. *International Journal of Solids and Structures*, 48(20): 2948–2959, 2011.
- 485 A. Panteghini and L. Bardella. On the compressive strength of glass microballoons-based syntactic foams. *Mechanics of Materials*, 82:63–77, 2015.
- A. Pedone, G. Malavasi, M. C. Menziani, U. Segre, and A. N. Cormack. Role of magnesium in soda-lime glasses: insight into structural, transport, and mechanical properties through computer simulations. *The Journal of Physical Chemistry C*, 112(29):11034–11041, 2008.
- M. Porfiri and N. Gupta. Effect of volume fraction and wall thickness on the elastic properties of hollow particle filled composites. 490 *Composites Part B: Engineering*, 40(2):166–173, 2009.
- A. Prakash and R. Lebensohn. Simulation of micromechanical behavior of polycrystals: finite elements versus fast fourier transforms. *Modelling and Simulation in Materials Science and Engineering*, 17(6):064010, 2009.
- F. Qi, H. Ding, X. Wang, Q. Liu, B. Du, and X. Zhang. The stress and strain field distribution around the reinforced particles in al/tic composites: A finite element modeling study. *Computational Materials Science*, 137:297–305, 2017.
- 505 C. Robert and C. Mareau. A comparison between different numerical methods for the modeling of polycrystalline materials with an elastic–viscoplastic behavior. *Computational Materials Science*, 103:134–144, 2015.
- W. S. Sanders and L. Gibson. Mechanics of hollow sphere foams. *Materials Science and Engineering: A*, 347(1-2):70–85, 2003.
- J. Segurado and J. Llorca. A numerical approximation to the elastic properties of sphere-reinforced composites. *Journal of the Mechanics and Physics of Solids*, 50(10):2107–2121, 2002.
- 500 A. Shams, A. Panteghini, L. Bardella, and M. Porfiri. A micromechanical model to study failure of polymer-glass syntactic foams at high strain rates. *Computational Materials Science*, 135:189–204, 2017.
- G. Tagliavia, M. Porfiri, and N. Gupta. Analysis of particle-to-particle elastic interactions in syntactic foams. *Mechanics of Materials*, 43(12):952–968, 2011.
- L. Wang, J. Lau, E. L. Thomas, and M. C. Boyce. Co-continuous composite materials for stiffness, strength, and energy 505 dissipation. *Advanced Materials*, 23(13):1524–1529, 2011.
- L. Weng, T. Fan, M. Wen, and Y. Shen. Three-dimensional multi-particle fe model and effects of interface damage, particle size and morphology on tensile behavior of particle reinforced composites. *Composite Structures*, 209:590–605, 2019.
- F. Willot. Fourier-based schemes for computing the mechanical response of composites with accurate local fields. *Comptes Rendus Mécanique*, 343(3):232–245, 2015.
- 510 M. Yu, P. Zhu, and Y. Ma. Effects of particle clustering on the tensile properties and failure mechanisms of hollow spheres filled syntactic foams: A numerical investigation by microstructure based modeling. *Materials & Design*, 47:80–89, 2013.
- X. Yu, J. Zhou, H. Liang, Z. Jiang, and L. Wu. Mechanical metamaterials associated with stiffness, rigidity and compressibility: A brief review. *Progress in Materials Science*, 94:114–173, 2018.
- 515 X. Zhang, P. Wang, Y. Zhou, X. Li, E.-H. Yang, T. Yu, and J. Yang. The effect of strain rate and filler volume fraction on the mechanical properties of hollow glass microsphere modified polymer. *Composites Part B: Engineering*, 101:53–63, 2016.